

Clustered Star Formation in Magnetic Clouds: Properties of Dense Cores Formed in Outflow-Driven Turbulence

Fumitaka Nakamura^{1,2}, Zhi-Yun Li³

Received _____; accepted _____

¹National Astronomical Observatory, Mitaka, Tokyo 181-8588, Japan; fumi-taka.nakamura@nao.ac.jp

²Institute of Space and Astronautical Science, Japan Aerospace Exploration Agency, 3-1-1 Yoshinodai, Sagami-hara, Kanagawa 229-8510, Japan

³Department of Astronomy, University of Virginia, P. O. Box 400325, Charlottesville, VA 22904; zl4h@virginia.edu

ABSTRACT

We investigate the physical properties of dense cores formed in turbulent, magnetized, parsec-scale clumps of molecular clouds, using three-dimensional numerical simulations that include protostellar outflow feedback. The dense cores are identified in the simulated density data cube through a clumpfind algorithm. We find that the core velocity dispersion does not show any clear dependence on the core size, in contrast to Larson’s linewidth-size relation, but consistent with recent observations. In the absence of a magnetic field, the majority of the cores have supersonic velocity dispersions. A moderately-strong magnetic field reduces the dispersion to a subsonic or at most transonic value typically. Most of the cores are out of virial equilibrium, with the external pressure dominating the self-gravity. The implication is that the core evolution is largely controlled by the outflow-driven turbulence. Even an initially-weak magnetic field can retard star formation significantly, because the field is amplified by the outflow-driven turbulence to an equipartition strength, with the distorted field component dominating the uniform one. In contrast, for a moderately-strong field, the uniform component remains dominant. Such a difference in the magnetic structure is evident in our simulated polarization maps of dust thermal emission; it provides a handle on the field strength. Recent polarization measurements show that the field lines in cluster-forming clumps are spatially well-ordered. It is indicative of a moderately-strong, dynamically important, field which, in combination with outflow feedback, can keep the rate of star formation in embedded clusters at the observationally-inferred, relatively-slow rate of several percent per free-fall time.

Subject headings: ISM: clouds — ISM: magnetic fields — MHD — polarization — stars: formation — turbulence

1. Introduction

Millimeter and submillimeter observations of dense cores in nearby parsec-scale cluster-forming clumps have shown that the core mass function (CMF) resembles the stellar initial mass function (IMF). For example, Motte et al. (1998) performed 1.2 mm continuum observations toward L1688 and identified 57 starless dense cores whose mass function ($dN/dM \sim M^{-2.5}$) is consistent with the Salpeter power-law IMF at the high mass end ($dN/dM \sim M^{-2.35}$). The CMF also has a break at about $0.3 M_{\odot}$, below which it flattens to $dN/dM \sim M^{-1.5}$. Other authors have found similar CMFs in the region (e.g., Johnstone et al. 2000; Stanke et al. 2006; Maruta et al. 2010). The shape of the CMF is broadly consistent with the IMF of Class II YSOs in the same region (Bontemps et al. 2001). Another example is the Serpens Cloud Core, where Testi & Sargent (1998) identified, through 3 mm continuum interferometric observations, 32 dense cores whose mass function can be fitted by a power-law of $dN/dM \sim M^{-2.1}$, again consistent with the Salpeter IMF. These and other observations suggest that the identified dense cores may be the direct progenitors of individual stars and the bulk of the stellar IMF may be at least partly determined by cloud fragmentation in the parsec-scale dense clumps. Thus, understanding the formation process of dense cores is a key step towards a full understanding of how stars form.

Both supersonic turbulence and magnetic fields are expected to play a role in clustered star formation. The relative importance of the two is still under debated, however. One school of thought is that the core (and thus star) formation in a cluster-forming clump is mainly regulated by supersonic turbulence. In this scenario, star formation is completed rapidly, before the initial supersonic turbulence has decayed significantly (e.g., Elmegreen 2000; Hartmann et al. 2001; Klessen et al. 2000). Magnetic fields are less important in this picture, although Padoan & Nordlund (2002) argued that a weak magnetic field is still

needed in order to produce a core mass spectrum that resembles the stellar IMF. The weak magnetic field is expected to be strongly tangled by the supersonic turbulence. Ordered field structures, if present at all, are typically attributed to large-scale compression and are expected to be parallel to the dense filaments that are also produced by the same compression (e.g., Pelkonen et al. 2007).

The second school of thought envisions a magnetic field that is more dynamically important; it prevents stars from forming too rapidly. Because supersonic turbulence dissipates rapidly, it must be somehow replenished. In a cluster-forming clump, protostellar outflow feedback can play an important role in turbulence regeneration (e.g., Maury et al. 2009; Arce et al. 2010; Nakamura et al. 2011a,b). Li & Nakamura (2006) demonstrated that protostellar outflows can resupply the supersonic turbulence, keeping the clumps near a quasi-virial equilibrium state for a relatively long time (see also Matzner 2007; Nakamura & Li 2007; Carroll et al. 2009). Because the matter moves preferentially along the dynamically important magnetic field, the field is expected to be more or less perpendicular to the dense filaments that are created by either turbulence compression or self-gravity. A goal of this paper is to quantify the effects of the magnetic field on the clustered star formation in general, and the properties of dense cores in particular, through 3D MHD simulations that include outflow feedback for turbulence replenishment.

The rest of the paper is organized as follows. In Section 2, we describe the numerical method and simulation setup. In Section 3, we apply a version of the so-called “clumpfind” algorithm to identify dense cores in a parent dense clump and derive their properties. We find that the internal motions of the cores are sensitive to the magnetic field strength of the parent clump and that the external surface pressures play a dominant role in core formation in outflow-driven turbulence. In Section 4, we compare the properties of the simulated cores with those observed in a couple of nearby cluster forming regions. Our main conclusions

are summarized in Section 5.

2. Model Formulation

The initial and boundary conditions of the simulations are essentially the same as those of Nakamura & Li (2007). We consider a centrally-condensed molecular gas clump inside a cubic simulation box of $L = 1.5$ pc on each side, with an initial density profile of $\rho(r) = \rho_0[1 + (r/r_c)^2]^{-1}$ for $r \leq L/2$ (where $r_c = L/6$ is the radius of the central plateau region) and $\rho(r) = 0.1\rho_0$ for $r > L/2$. Here, the central density ρ_0 is given by $\rho_0 = 4.68 \times 10^{-24}n_{\text{H}_2,0}$ g cm $^{-3}$, with $n_{\text{H}_2,0}$ being the central number density of molecular hydrogen, assuming 1 He for every 10 H atoms. Periodic boundary condition is applied to each side of the box. We adopt a central H $_2$ density of $n_{\text{H}_2,0} = 2.69 \times 10^4(T/20 \text{ K})(1.5 \text{ pc}/L)^2$ cm $^{-3}$, corresponding to a central free-fall time $t_{\text{ff},c} = 0.19$ Myr and a central Jeans length of $L_J = (\pi c_s^2/G\rho_0)^{1/2} \simeq 0.17(T/20\text{K})^{1/2}(n_{\text{H}_2,0}/2.69 \times 10^4\text{cm}^{-3})^{-1/2}$ pc. It yields a total clump mass of $M_{\text{tot}} = 939M_\odot$. The average clump density is $n_{\text{H}_2}^- = 4.0 \times 10^3$ cm $^{-3}$, corresponding to a global free-fall time $t_{\text{ff},cl} = 0.49$ Myr. An isothermal equation of state is assumed, with a sound speed of $c_s = 0.266$ km s $^{-1}$ for gas temperature $T = 20$ K.

Our choice of the clump mass, density and gas temperature is motivated by observations of the nearest pc-scale cluster forming clump, the ρ Ophiuchi main cloud. From ^{13}CO ($J = 1 - 0$) observations, Loren (1989) estimated a total gas mass of $865 M_\odot$ for the whole L1688 region, adjusted for the parallax distance of 125 pc (e.g., Lombardi et al. 2008; Loinard et al. 2008). The gas temperature in the region has some spatial variation, but the average appears close to 20 K. Our clump parameters are also consistent with those of other nearby cluster-forming clumps (Ridge et al. 2003) and the infrared dark clouds which are thought to be future sites of cluster formation in GMCs (e.g., Butler & Tan 2009).

At the beginning of the simulation, we impose on the clump a uniform magnetic field along the x -axis. The field strength is specified by the plasma β , the ratio of thermal to magnetic pressures at the clump center, through $B_0 = 47\beta^{-1/2}(T/20\text{K})^{1/2}(n_{\text{H}_2,0}/2.69 \times 10^4\text{cm}^{-3})^{1/2} \mu\text{G}$. In units of the critical value $1/(2\pi G^{1/2})$ (Nakano & Nakamura 1978), the mass-to-flux ratio in the central flux tube is given by $\lambda_0 \simeq 8.3\beta^{1/2}$. The mass-to-flux ratio for the clump as a whole is $\bar{\lambda} \simeq 3.0\beta^{1/2}$. Although systematic measurements of magnetic field strength in cluster-forming clumps are not available, relatively strong magnetic fields are inferred in some cases: e.g., 850 μG for OMC 1 at $n \sim 10^{5-6} \text{cm}^{-3}$ (see Crutcher 1999; Houde et al. 2004; Nakamura & Li 2007) and 160 μG for Serpens at $n_{\text{H}_2,0} \sim 10^{4-5} \text{cm}^{-3}$ (Sugitani et al. 2010). In the present paper, we adopt as a representative value $\beta = 0.2$ (or 100 μG at $n_{\text{H}_2} \sim 3 \times 10^4 \text{cm}^{-3}$), corresponding to $\bar{\lambda} \simeq 1.4$ or a dimensionless flux-to-mass ratio $\bar{\Gamma} \simeq 0.74$, so that the clump as a whole, as well as the denser central region, is magnetically supercritical.

Following the standard practice (e.g., Mac Low et al. 1998; Ostriker et al. 2001), we stir the initial clump at the beginning of the simulation with a turbulent velocity field of power spectrum $v_k \propto k^{-4}$ and rms Mach number $\mathcal{M} = 5$. Our initial clump has a virial parameter (the ratio of the kinetic energy to the gravitational energy) of $\alpha_{\text{vir}} \simeq 0.5$. The effective α_{vir} should be close to unity for $\bar{\Gamma} \simeq 0.74$ since the gravitational energy is effectively reduced by the magnetic field by a factor of $1 - \bar{\Gamma}^2$. The turbulence is allowed to decay freely, except for feedback from protostellar outflows.

The evolution of the turbulent, magnetized molecular clump is followed using a three-dimensional MHD code based on an upwind TVD scheme. The MHD code is essentially the same as those used in Li & Nakamura (2006) and Nakamura & Li (2007). The ideal MHD equations are solved using the code having second-order accuracy in both space and time. The equation of state is assumed to be isothermal. To ensure the divergence-free magnetic

field, the divergence cleaning method is adopted. The Poisson equation for gravitational potential is solved using the fast Fourier transform. Our simulation has a resolution of 256^3 . Although our focus is on core properties, we do include a crude treatment of the formed stars and outflows, following Nakamura & Li (2007); we refer the reader to that paper for details. Briefly, when the density in a cell crosses the threshold $\rho_{\text{th}} = 400\rho_0$, corresponding to 10^7 cm^{-3} , we create a Lagrangian particle at the cell center. We extract mass from a small region surrounding the cell, and put it on the particle, which moves with mass-weighted mean velocity of the extracted mass (see Nakamura & Li 2007 for more detail). After creation, the particle is allowed to accrete from the surrounding gas according to the same prescription as Wang et al. (2010). To mimic the effect of protostellar outflows, the particle injects into the ambient gas a momentum that is proportional to the particle mass increment ΔM_* . The outflow momentum is scaled with the dimensionless outflow parameter f as $P = f(\Delta M_*/M_\odot)(V_w/100\text{km s}^{-1})$, where V_w is the wind velocity (see the Appendix of Nakamura & Li 2007). The fiducial value of f is set to 0.4, consistent with Matzner & McKee (2000). Each outflow has a bipolar and spherical component, with a momentum ratio of 3:1. The model parameters are summarized in Table 1.

3. Numerical Results

We first concentrate on the dense cores identified in three representative models: model N1 (no magnetic field, $\beta = \infty$), W1 (weak magnetic field, $\beta = 2$), and S1 (moderately-strong magnetic field, $\beta = 0.2$). Their dimensionless outflow parameter is set to the fiducial value $f = 0.4$.

3.1. Core Identification

Following Nakamura & Li (2008), we identify dense cores from the density data cube using a variant of the CLUMPFIND algorithm of Williams et al. (1994). We adopt a threshold density $\rho_{\text{th,min}} = 4\rho_0$ ($\sim 10^5 \text{ cm}^{-3}$), and a maximum density $\rho_{\text{th,max}} = 400 \rho_0$ ($\sim 10^7 \text{ cm}^{-3}$, above which a Lagrangian particle is created). Thus, the cores identified from our simulation data correspond roughly to the dense cores observed in the dust continuum emission and high density molecular tracers such as N_2H^+ ($J = 1 - 0$) and H^{13}CO^+ ($J = 1 - 0$). The density distribution between $\rho_{\text{th,min}}$ and $\rho_{\text{th,max}}$ is divided into 10 bins equally spaced logarithmically. We include only those spatially resolved cores containing more than 50 cells in the analysis, to ensure that their properties are determined with reasonable accuracy. We also choose the cores that do not include particles. In this sense, our identified cores correspond to starless cores. The minimum core mass and radius identified through this procedure are $M_{\text{c,min}} \equiv \rho_{\text{th,min}} \times 50\Delta x\Delta y\Delta z \sim 0.05M_\odot$ and $\sim 0.01 \text{ pc}$, respectively. We note that our core identification procedure is not exactly the same as those used in observational studies, which are typically based on position-position-velocity data cubes of molecular line emission or column density maps from dust continuum emission.

3.2. Spatial Distribution of Dense Gas

Before discussing the physical properties of the identified cores, we show how the magnetic field affects the global density distribution. Figure 1 compares the column density distributions along the y -axis for the three models with different initial magnetic field strengths, at a stage when the star formation efficiency has reached 16%. Since the star formation is retarded by the magnetic field, the evolution time tends to be longer at a given SFE for a stronger magnetic field. For comparison, the positions of the formed stars

and the identified dense cores projected on the $x - z$ plane are indicated by the dots and triangles, respectively, in Fig. 1. The initial magnetic field direction is parallel to the x -axis (the abscissa).

Figure 1 indicates that the global density distribution depends on the initial magnetic field strength. For the non-magnetic model (model N1), the global density distribution shows a large-scale filamentary structure that contains many small fragments (Figs. 1a and 1d). The formation of the large-scale filament is probably because the turbulence energy is initially highest on the largest scale and the large-scale compression may be further amplified by self-gravity to create the filamentary structure.

For the weakly-magnetized case (model W1), the global density distribution does not clearly show a large-scale filamentary structure by the stage shown in Figs. 1b and 1e. The dense part appears to contain many smaller filaments or elongated fragments that are distributed almost independently of the initial magnetic field direction. This is different from the non-magnetic case. The difference may be because the local turbulent motions amplify random magnetic field components (see Section 4.2), which slow down the formation of the large-scale filamentary structure.

In contrast, in the presence of a moderately-strong magnetic field (model S1), the cloud material condenses preferentially along the magnetic field lines into a large-scale filamentary structure that is nearly perpendicular to the initial magnetic field direction. Several less-dense filaments are also associated with the large-scale filament (hereafter the main filament). The less-dense filaments appear to be more or less along the initial magnetic field direction and to merge toward the dense parts of the main filament. The dense cores are distributed primarily along the main filament. The column density distribution is reminiscent of the hub-filament structures of star forming regions pointed out by Myers (2009). The observed hub-filament structures may indicate the presence of the

moderately-strong, spatially-ordered magnetic field, instead of the weak magnetic field that are tangled by supersonic turbulence. We will revisit this issue in Section 4.3, where we compare dust polarization maps derived from the simulation data for models W1 and S1.

3.3. Core Property

As shown in Li & Nakamura (2006) and Nakamura & Li (2007), our model clump has reached a quasi-equilibrium state within one global free-fall time. After that, the statistical properties of the cores remain largely-unaltered. Therefore, to compare the statistical properties of the identified cores, we choose the same stage as that of Fig. 1, i.e., the stage when 16 % of the total mass has been converted into stars. In this subsection, we compare the core properties for the three representative models, models N1, W1, and S1. The total numbers of identified cores are 160, 105, and 105 cores for models N1, W1, and S1, respectively.

3.3.1. Radius, Mass, and Velocity Dispersion

We now focus on the physical properties of the cores identified in the three representative models. To facilitate comparison with observations, we present the core properties in dimensional units. Figures 2a through 2i show the histograms of the core radius, mass, and velocity dispersion of the nonthermal component. The minimum, maximum, mean, and median values are summarized in Table 2. The core radius, R_c , is defined as the radius of a sphere having the same volume as the core. The distributions of core radius are broadly similar in all cases. They range from ~ 0.01 pc to ~ 0.05 pc, all peaking around 0.02 pc. The maximum and mean core radii are somewhat larger in model S1 (the moderately-strong field case) than in the other two. The core mass distribution shows a similar trend. In all

models, the core mass ranges from $\sim 0.07 M_{\odot}$ to $\sim 4M_{\odot}$. The mean value is somewhat larger for model S1 than for the other two. The mean core mass and radius are larger in model S1 probably because the stronger magnetic field can support more mass against gravitational collapse.

The magnetic effect is even more prominent in the distribution of core velocity dispersion. For the non-magnetic model (model N1), the velocity dispersion ranges from $\sim 0.1 \text{ km s}^{-1}$ to 4 km s^{-1} , peaking around 1 km s^{-1} (corresponding to a Mach number of ~ 4). Most of the cores have supersonic internal motions in this case, which appears inconsistent with the predominantly subsonic or at most transonic internal motions inferred observationally (e.g., Andre et al. 2007; Walsh et al. 2007; Maruta et al. 2010, see also Section 4.1). Even a relatively weak magnetic field appears to affect the internal motions inside the cores significantly. For model W1, the median velocity dispersion is estimated at $\sim 0.5 \text{ km s}^{-1}$, corresponding to a Mach number of about 2, although the mean is almost the same as that of model N1. Most of the cores in this case still have supersonic velocity dispersions.

In contrast, for model S1, the majority of the cores have a velocity dispersion close to, or less than, $\sim 0.3 \text{ km s}^{-1}$, which is comparable to the sound speed ($c_s = 0.266 \text{ km s}^{-1}$). The velocity dispersion ranges from $\sim 0.05 \text{ km s}^{-1}$ to 2 km s^{-1} , peaking around the median of 0.3 km s^{-1} . In other words, the strong magnetic field tends to reduce the core internal motions significantly. The reduction is probably because the magnetic field cushions the converging flows in the supersonic turbulence that are largely responsible for the core formation. The magnetic effect is also evident in the virial state of the cores, as we show below.

3.3.2. Velocity Dispersion-Radius Relation

The internal motions of the observed dense cores are often measured using the velocity dispersions derived from molecular line data. Here, we compare the velocity dispersions for the three representative models with different field strengths to study the effects of the magnetic field.

Figure 3 plots the non-thermal components of 3D velocity dispersions of the identified cores against the core radii for (a) model N1, (b) model W1, and (c) model S1. The best-fit power-laws are given by $(\Delta V_{\text{NT}}/\text{km s}^{-1}) = (2.2 \pm 1.9)(R_c/\text{pc})^{0.19 \pm 0.22}$ ($\mathcal{R} = 0.023$), $(\Delta V_{\text{NT}}/\text{km s}^{-1}) = (3.8 \pm 9.0)(R_c/\text{pc})^{0.35 \pm 0.61}$ ($\mathcal{R} = 0.070$), and $(\Delta V_{\text{NT}}/\text{km s}^{-1}) = (1.1 \pm 0.48)(R_c/\text{pc})^{-0.34 \pm 0.12}$ ($\mathcal{R} = 0.29$) for models N1, W1, and S1, respectively, where \mathcal{R} denotes the correlation coefficient. It shows that there is no clear correlation between the velocity dispersion and core radius. Our cores do not follow the power-law linewidth-radius relation derived by Larson (1981). The same conclusion holds for dense cores formed in even more strongly magnetized, magnetically subcritical, clouds (see Figure 18 of Nakamura & Li 2008). The reason is probably that the dense cores created out of turbulent molecular gas are generally not in virial equilibrium (the equilibrium is implied by Larson’s laws) and that their formation is strongly influenced by external turbulent flows (see below).

Quantitatively, the velocity dispersions of the cores depend on the initial magnetic field strength, as shown already in Figs. 2g through 2i. In the absence of magnetic field (model N1), about 40% of the cores have velocity dispersions larger than 1 km s^{-1} ; the majority of the cores have supersonic internal motions. As mentioned above, even a relatively weak magnetic field can influence the internal motions significantly. In model W1, although many cores still have large velocity dispersions, the median value is less than that in model N1 by a factor of ~ 2 . In the stronger field case (model S1), the median and mean of the velocity dispersions are estimated at 0.31 and 0.46 km s^{-1} . About 40 % of the cores have velocity

dispersions smaller than the sound speed of 0.266 km s^{-1} ; the majority of the cores have subsonic or at most transonic internal motions, which is more consistent with observations. We conclude that the magnetic field plays a significant role in reducing the internal motions of the cores.

3.3.3. Virial Parameter

The virial parameter, the ratio of the virial mass to core mass, is often used as a measure of the gravitational boundedness of dense molecular cloud cores, particularly in observational studies. In Fig. 4, we plot the virial parameters against the core mass for the three models. Here, we calculate the virial parameter as

$$\alpha_{\text{vir}} = \frac{5\Delta V_{\text{1D}}^2 R_c}{GM_c}, \quad (1)$$

where ΔV_{1D} is the 1D FWHM velocity width including thermal contribution and the virial mass of each core is obtained by assuming that it is a uniform sphere. The virial mass depends on the density distribution. For a centrally condense sphere with $\rho \propto r^{-2}$, the virial parameter is reduced by a factor of $5/3$. Note that the effects of the nonspherical mass distribution appear to be small as long as the aspect ratios of the cores are not far from unity (Bertoldi & McKee 1992).

Figure 4 indicates that the relationship between the virial parameter and core mass depends on the initial magnetic field strength. In the absence of a magnetic field (model N1), the virial parameters are typically very large, and have a large scatter. The scatter in the virial parameter-mass plot comes mainly from the large scatter in the velocity dispersion-radius relation (see Fig. 3). The virial parameters often exceed $10 - 10^2$ even for relatively massive cores, indicating that, for most of the cores, the gravitational energy is much smaller than the internal kinetic energy. The virial parameters tend to increase

with decreasing core mass, and the lower bound of the virial parameters follows roughly a power-law relation of $\alpha_{\text{vir}} \propto M_c^{-2/3}$.

For the model with a weak magnetic field (model W1), the virial parameter-mass relation is qualitatively similar to that of the non-magnetized model (model N1). Although the fraction of cores with large virial parameters is somewhat small for the weak magnetic field case, the scatter in the virial parameter-mass relation remains large. About 30 % of the cores still have virial parameters larger than 10.

On the other hand, for the model with a moderately-strong magnetic field (model S1), the identified cores tend to follow a single power-law relation of $\alpha_{\text{vir}} \propto M_c^{-2/3}$, with a rather small scatter. Furthermore, most of the cores (about 9 % of the cores) have virial parameters smaller than 10. This trend is consistent with the initially-magnetically subcritical case (see Figure 17 of Nakamura & Li 2008). It is also in good agreement with the scaling found by Bertoldi & McKee (1992) for nearby giant molecular clouds. According to Bertoldi & McKee (1992), an object confined by the ambient pressure has a virial ratio that is proportional to $(M_c/M_J)^{-2/3}$, where M_J is the Jeans mass defined by Equation (2.13) of Bertoldi & McKee (1992). The fact that our cores follow the same relation implies that the ambient pressure plays an important role in confining our cores as well. In the next subsection, we perform a detailed virial analysis of the cores to quantitatively clarify the role of the surface pressure term in core dynamics.

3.3.4. *Virial Analysis*

The virial theorem is useful for analyzing the core dynamical properties. Here, we perform a detailed virial analysis using the virial equation in Eulerian coordinates (e.g.,

McKee & Zweibel 1992; Tilley & Pudritz 2007; Dib et al. 2007)

$$S = \frac{1}{2}\ddot{I} + \frac{1}{2}\frac{d}{dt}\int_S \rho r^2 \mathbf{v} \cdot d\mathbf{S} = U + K + M + W + S + F, \quad (2)$$

where $I = \int_V \rho r^2 dV$, $U = 3 \int_V P dV$, $K = \int_V \rho v^2 dV$, $W = - \int_V \rho \mathbf{r} \cdot \nabla \Psi dV$, $M = (1/8\pi) \int_V B^2 dV$, $S = - \int_S [P \mathbf{r} + \mathbf{r} \cdot (\rho \mathbf{r} \mathbf{r})] \cdot d\mathbf{S}$, and $F = \int_S \mathbf{r} \cdot \mathbf{T}_M \cdot d\mathbf{S}$. The quantities I , U , K , W , S , M , F , and \mathbf{T}_M denote, respectively, the moment of inertia, internal thermal energy, internal kinetic energy, gravitational energy, the sum of the thermal surface pressure and dynamical surface pressure, internal magnetic energy, the magnetic surface pressure, and the Maxwell stress-energy tensor. The internal thermal, kinetic, and magnetic energies are always positive. Other terms can be either positive or negative. In particular, the gravitational term can be positive in crowded environments where the background gravitational field dominates the core dynamics (see e.g., Ballesteros-Paredes et al. 2009). In fact, as shown below, several cores have positive gravitational terms in our simulations, although no cores have positive gravitational terms for the initially magnetically subcritical case where the turbulent motions are not so strong because of the effects of magnetic cushion (see Fig. 16 of Nakamura & Li 2008). The second term on the left-hand side of equation (2) denotes the time derivative of the flux of moment of inertia through the core boundary. As is the standard practice (Tilley & Pudritz 2007; Dib et al. 2007; Nakamura & Li 2008), we ignore the left-hand side of equation (2) in our discussion and consider a core to be in virial equilibrium if the sum $U + K + W + S + M + F = 0$.

The equilibrium line is shown in Figure 5, where the sum of the surface terms ($S + F$) is plotted against the gravitational term (W), both normalized to the sum of the internal terms ($U + K + M$). For the surface term, the external kinetic term is generally much larger than the magnetic term (F).

For all three models, the majority of the cores lie below the virial equilibrium line, and thus they are expected to be unstable to contraction. In addition, the surface term

appears more important than the gravitational term for most of the cores. In the absence of the magnetic field, about 10 – 20 % of the cores have the normalized surface term of $|S + F|/|U + K + M| \gtrsim 5$, whereas no cores have the normalized surface term of $|S + F|/|U + K + M| \gtrsim 5$ in the presence of the moderately-strong magnetic field. The magnetic field tends to reduce the contribution of the surface terms to the core dynamical state, although the surface term is still dominant even in the presence of the strong magnetic field.

The core virial state is in contrast to the initially-magnetically subcritical case. For the initially-magnetically subcritical case, for most of the cores, the surface term ($S + F$) and gravitational term (W) tend to be smaller than the sum of the internal terms, $U + K + M$ (Nakamura & Li 2008), and thus most of the cores are distributed around the virial equilibrium line. In addition, more massive cores tend to be distributed below the virial equilibrium line, and the importance of the self-gravity tends to depend on the core mass. The gravitational term tends to be more important for more massive cores for the initially magnetically subcritical case, implying that the gravitational collapse induced by ambipolar diffusion regulates the core evolution. In contrast, for the magnetically-supercritical cases studied in this paper, most of the cores are distributed further from the virial equilibrium line. The surface term ($S + F$) tends to be larger than the sum of the internal terms, $U + K + M$ for most of the cores. The core virial state shows no clear dependence on the mass. The surface term, which is typically dominated by the ambient supersonic turbulence, is still important even for massive cores.

The above result is different from that of Tilley & Pudritz (2007). They found, in their ideal MHD simulations, a larger contribution from the surface term to the virial equation for a stronger magnetic field, which is opposite to the trend we found. This difference likely comes from the fact that they only followed the very early phase of cloud evolution, when

the initial supersonic turbulence has decayed significantly but star formation has yet to set in. Most of our cores are formed at much later times, after the decayed turbulence has been replenished by outflow feedback. Given this difference, it is perhaps not too surprising that the surface terms are much larger in our models than in theirs. This is particularly true for the weaker magnetic field case, because of a more rapid and violent star formation.

In our simulations, most of the identified cores have the densities smaller than the critical density beyond which the Jeans condition is violated. For example, the Jeans condition is satisfied for 89 % (model N1), 85 % (model W1), and 95 % (model S1) of the cores presented in this subsection. For the stronger initial magnetic field, the mean density of the cores tend to be smaller due to the magnetic support, and therefore the Jeans condition is satisfied for a larger number of cores. We also performed a run with 512^3 for model S1, with the threshold density fixed, so that the Jeans condition is always satisfied in the entire computation box. To compare directly with the results presented in this subsection, we first resized the data obtained from the 512^3 run to the 256^3 grid data, and then applied the clumpfind method to the regridded data. We confirmed that the statistical properties of the identified cores are essentially the same as those presented in this subsection. For example, for all the cores identified from the 512^3 data, the nonthermal 3D velocity dispersions of the identified cores stay below 1 km s^{-1} , and its mean is estimated to be 0.43 km s^{-1} , comparable to that of the 256^3 data, 0.46 km s^{-1} .

3.4. Effects of Outflow Strength

After exploring the effects of the magnetic field on the core properties, we now turn to the outflow strength. In our model, the strength of the outflow feedback is specified by the dimensionless parameter, f . This parameter is highly uncertain because it is generally difficult to determine the physical properties of molecular outflows accurately

from observational data. In this paper, we adopt $f = 0.4$ as a fiducial value, following Matzner & McKee (2000). Recently, Nakamura et al. (2011) discovered many molecular outflow lobes toward an extremely-young cluster-forming clump, Serpens South, on the basis of CO ($J = 3 - 2$) observations, and derived the physical properties of the identified molecular outflows. They roughly estimated $f \sim 0.1 - 0.3$ for these outflows, assuming that the outflow gas is optically-thin. If a substantial amount of the outflow gas is optically-thick, the outflow parameter f would be larger. In the following, we compare the core properties of three models with different outflow strengths: $f = 0, 0.1, \text{ and } 0.4$. The fiducial value for plasma β of 0.2 is adopted for these models.

In Figs. 6a through 6c, we compare the velocity dispersion-radius relations for the moderately-strong magnetic models with no outflow feedback ($f = 0$), weak outflow ($f = 0.1$), and strong outflow ($f = 0.4$). In the model with no outflow feedback (model S3), the number of identified cores is smaller than in the other two models, and the mean core mass tends to be slightly larger. This difference may be due to the fact that the ambient turbulent motions are weaker without any outflow feedback and thus the turbulent fragmentation does not form smaller-scale structures as efficiently. Figure 6 indicates that the velocity dispersion-radius relation does not depend strongly on the strength of the outflow feedback. For all three models, there is no clear relationship between the velocity dispersion and the core radius. Thus, it appears difficult to discriminate the effects of protostellar outflows based on the velocity dispersion-radius relation alone.

The surface term-gravitational term plots in Figs. 7a through 7c indicate that the dynamical states of the cores depend somewhat on the outflow strength. In the absence of the outflow feedback, more cores are located near the dashed line (where the two terms are equal). The gravitational term appears more important for this model than for the other two, although the surface term is clearly still important. This is due, at least in part, to

the fact that the global gravitational infall can generate fast motions even in the absence of protostellar outflow driven turbulence.

It is difficult, however, to gauge the effects of the outflow feedback from the virial parameters of the cores, which are often used in observational studies of the molecular cloud cores in star-forming molecular clouds. The difficulty is illustrated in Figs. 8a through 8c, where we show the virial parameter-mass relations for the three models with different outflow strengths. In all cases, the distributions of the virial parameters are similar, following a power-law of $\alpha_{\text{vir}} \propto M_c^{-2/3}$ with rather small dispersions.

3.5. Outflow Direction

In this subsection, we investigate how well the outflow axes are aligned with the global or initial magnetic field direction in parsec-scale cluster forming clumps. In our simulations, the outflow direction is set to the local magnetic field direction at the position of each formed star. This should be a reasonable approximation since the outflows are most likely driven along the local magnetic field by field line twisting due to disk rotation, (e.g., Matsumoto et al. 2006).

Figure 9 shows the histogram of the outflow direction as a function of the angle between the outflow axis and the initial magnetic field direction, for the model with a moderately-strong magnetic field (model S1). All the outflows created by the time when $SFE \simeq 0.16$ are shown. The outflow direction shows a broad distribution, taking its maximum at the mean angle of about 30° . The conclusion is that, although there is some preference for the outflows to align with the global magnetic field direction, the alignment is not as strong as one may naively expect. This is because most of the dense cores are formed through outflow-induced turbulent compression, which can push the magnetic field

on the core scale away from the global field direction. On smaller scales, the misalignment in field direction can be further amplified by gravitational collapse. The lack of a complete alignment between the outflow axes and the global field direction is thus expected. It can not be used to argue against the presence of a moderately-strong global magnetic field.

4. Discussion

4.1. Comparison with Core Observations

Here, we compare the core properties obtained in Section 3 with observations. We use the core data toward two nearby parsec-scale cluster-forming clumps: the ρ Ophiuchus Main Cloud and NGC 1333 in Perseus. In the ρ Ophiuchus region, Maruta et al. (2010) identified 68 H^{13}CO^+ ($J = 1 - 0$) cores by applying clumpfind to the 3D position-position-velocity cube data obtained using Nobeyama 45 m telescope. In NGC 1333, Walsh et al. (2007) identified 93 N_2H^+ ($J = 1 - 0$) dense cores, again using clumpfind. Since both the H^{13}CO^+ ($J = 1 - 0$) and N_2H^+ ($J = 1 - 0$) transitions have critical densities of order $\sim 10^5 \text{ cm}^{-3}$, the H^{13}CO^+ and N_2H^+ cores should have densities comparable to our simulated cores, which were identified using a threshold density $\sim 10^5 \text{ cm}^{-3}$. Since the moderately-strong field model yields a core velocity dispersion that is in better general agreement with observations than the non-magnetic or weak-field model, we will concentrate on comparing its cores with the ρ Oph and NGC 1333 data.

In Fig. 10a, we compare the 1D FWHM nonthermal velocity width-radius relations for the ρ Oph cores of Maruta et al. (2010) and our simulated cores (see Section 3). The 3D velocity dispersions discussed in Section 3 was converted into the 1D FWHM velocity widths using $dV_{\text{NT}} = (8 \ln 2/3)^{1/2} \Delta V_{\text{NT}}$. Our simulated cores tend to be somewhat smaller than the ρ Oph cores; the average radius of the ρ Oph cores is estimated at 0.04 pc, about

1.7 times that of model S1. Aside from the size difference, the observed and simulated data are almost indistinguishable. Neither shows a clear dependence of linewidth with size, except for a weak trend for the linewidth to increase slightly with radius. Neither follows the Larson’s linewidth-size relation. The observations are also consistent with the cores formed from initially-magnetically subcritical clouds (see Fig. 18 of Nakamura & Li 2008). We did not plot the NGC 1333 cores on Fig. 10a because the core radius in Table 1 of Walsh et al. (2007) was quoted in single significant digit, which artificially introduces a large scatter in the plot. Nevertheless, inspection by eye reveals no clear correlation between the velocity width and core radius, broadly consistent with the data for both the ρ Oph cores and the simulated cores of model S1.

Figure 10b compares the virial parameter-mass relations of the simulated and observed cores. The red and blue dots, and black crosses denotes the ρ Oph (Maruta et al. 2010) and NGC 1333 cores (Walsh et al. 2007), and the cores of model S1, respectively. For the NGC 1333 cores, we recalculated the virial masses by including the thermal contribution from the gas with a temperature of 15 K and adopting a distance of 235 pc (Hirota et al. 2008), instead of 300 pc used in Walsh et al. (2007). We also recalculated the LTE masses by adopting the N_2H^+ fractional abundance relative to H_2 of $X_{\text{N}_2\text{H}^+} \sim 3 \times 10^{-10}$ derived from observations toward ρ Oph because Walsh et al. (2007) determined their adopted N_2H^+ fractional abundance such that the points are distributed evenly about the line of equality ($M_{\text{LTE}} = M_{\text{vir}}$) in their $M_{\text{LTE}}-M_{\text{vir}}$ plot. This N_2H^+ fractional abundance is determined by taking average of the values obtained toward Oph A (Di Francesco et al. 2004) and B2 subclumps (Friesen et al. 2010). Figure 10b indicates that the virial parameter-core mass relation of the nearby cluster-forming clumps follows roughly a single power-law of $\alpha_{\text{vir}} \propto M_c^{-2/3}$ with a small dispersion, which is again in good agreement with model S1 that has a moderately-strong magnetic field. A dynamically important magnetic field may have played a role in core formation in these regions.

Besides the ρ Oph region, Maruta et al. (2010) found that the velocity dispersions of H^{13}CO^+ cores are almost independent of the core radius in Orion A as well, even though the latter is more than a factor of 3 farther away. The coarser spatial resolution for Orion means that its cores may contain (smaller, ρ Oph-like) cores blending together. If this is true, then the nearly flat velocity-width-radius relation observed in both regions suggests that the inter-core motions among the neighboring cores are almost comparable to the internal motions in the individual cores. Such a feature was pointed out by André et al. (2007) who measured the velocity difference among neighboring cores using N_2H^+ ($J = 1 - 0$). If the velocity-width-radius relation is flat ($\Delta V \propto \text{constant}$) and the core mass is proportional to R_c^3 , then the virial parameter is scaled as $\alpha_{\text{vir}} \propto R_c \Delta V^2 / (GM_c) \propto M_c^{-2/3}$, a similar power-law to that derived by Bertoldi & McKee (1992). This again suggests the importance of ambient turbulent pressure in dynamics of the cores as discussed in Section 3.

4.2. Amplification of Magnetic Field

To isolate the effect of magnetic field on clustered star formation, we present in Fig. 11a the time evolution of star formation efficiency (SFE) for three models with different field strengths but no outflow feedback. Our simulations show that, as expected, the magnetic field tends to slow down star formation, especially at relatively late times. The rate of star formation remains rather high, however, particularly at early times. For example, from the formation of the first star to the time when the SFE reaches $\sim 16\%$, the average star formation efficiency per global free-fall time (SFR_{ff} ; Krumholz & McKee 2005) is estimated to be 29 %, 27 %, and 21 %, respectively, for models N2, W2, and S2. These values are larger than the observationally inferred values of a few % (Krumholz & Tan 2007). The large SFR_{ff} in the absence of outflow feedback is in agreement with previous studies (see also the Appendix for the analytic formula of SFR_{ff}). For example, using MHD SPH

simulations, Price & Bate (2008) and Price & Bate (2009) followed the evolution of $50 M_{\odot}$ clumps with $0.25 \leq \beta \leq \infty$ until $t \lesssim 1.5t_{\text{ff,cl}}$. Although their initial model clump mass is too small compared to nearby cluster-forming clumps like ρ Oph and NGC 1333 (which have masses of order $10^3 M_{\odot}$), their star formation efficiencies per free-fall time are estimated to be over 10 %. These simulations imply that it is difficult to reduce the star formation rate to the observed level by a moderately-strong magnetic field alone, and other factors are needed to significantly retard star formation in cluster-forming clumps.

One way to slow down star formation is the feedback from forming stars. Price & Bate (2009) found that radiative feedback from forming stars does not change the global star formation efficiency in a parent clump much, although it significantly suppresses the small-scale fragmentation by increasing the temperature in the high-density material near the protostars. Figure 11b shows that the star formation rate is greatly reduced by the inclusion of outflow feedback, even in the presence of a relatively weak magnetic field, in agreement with previous studies (Li & Nakamura 2006; Nakamura & Li 2007; Wang et al. 2010). The average star formation efficiency per global free-fall time is estimated to be 8 %, 6 %, and 4 % for model N1 (no magnetic field), W1 (weak field), and S1 (moderately-strong field), respectively. For the model with the moderately-strong field, the SFR_{ff} is more or less comparable to the observed value.

The reason for the large reduction in SFR_{ff} can be seen in Fig. 12, where the magnetic energy is plotted against the evolution time, for models W1 and S1. As shown in Fig. 12a, for the moderately-strong field case, the total magnetic energy is dominated by the background uniform field that does not contribute to the force balance in the initial cloud. We therefore illustrate in Fig. 12b the time evolution of the magnetic energy stored in the distorted component that was amplified by supersonic turbulence. Here, we computed the magnetic energy stored in the distorted component by subtracting the initial

magnetic energy from the total magnetic energy. For comparison, we also plotted in Fig. 12b the evolution of the total kinetic energy of the clump. Since the kinetic energy is often dominated by the unbound high-velocity gas associated with the active outflows, we approximate the total kinetic energy of the clump as the kinetic energy of the gas whose velocity is smaller than $10 c_s$. For both models, the amplified components tend to increase with time. For the model with the moderately-strong field, the amplified component begins to oscillate around a level value after a free-fall time. For both models, the magnetic energy of the amplified component becomes comparable to the kinetic energy of the dense gas by the end of the computation, indicating that a quasi-equipartition has been reached (see also Federrath et al. 2011). For the weak field case, the amplified component is more important than the initial uniform field, resulting in a significantly-distorted magnetic field structure. Such a highly-distorted magnetic field can be seen in the 3D bird’s eye view of the density and magnetic field distributions of model W1, which is presented in the left panel of Fig. 13. In contrast, the global magnetic field is well-ordered for the case of moderately-strong initial magnetic field, which is shown in the right panel of Fig. 13.

4.3. Polarization Maps

Polarization maps of submillimeter thermal dust emission have recently been obtained for nearby star forming regions (e.g., Houde et al. 2004; Girart et al. 2009; Matthews et al. 2009). Here, we present the polarization maps derived from the simulation data for the two magnetically-supercritical models with different initial magnetic field strengths (models W1 and S1 which have the magnetic flux-to-mass ratios of $\bar{\lambda} = 4.3$ and 1.4, respectively). We computed the polarized thermal dust emission from the MHD model following Padoan et al. (2001). We neglect the effect of self-absorption and scattering because we are interested in the thermal dust emission at submillimeter wavelengths. We further assume that the grain

properties are constant and the temperature is uniform. The polarization degree is set such that the maximum is equal to 15 %. Figure 14 shows the dust polarization maps calculated from models W1 and S1.

Only a small portion of the computation box is shown in each panel of Fig. 14. As expected from Fig. 13, in the presence of a weak magnetic field, the spatial distribution of the polarization vectors has relatively large fluctuations. The polarization degree tends to be smaller in several parts where the magnetic fields are strongly distorted. In the densest parts, the polarization vectors appear more or less parallel to the local elongated structures or dense filaments, whereas there is no clear correlation between the vectors and density distribution in less dense parts. This may be due to the fact that the local dense filaments are created by turbulent compression that preferentially enhances the magnetic field component transverse to the shock plane. In contrast, in the presence of the strong magnetic field, the filamentary structure is prominent and the filament axes tend to be perpendicular to the polarization vectors that are almost parallel to the initial magnetic field direction, suggesting that the gas flow is channeled preferentially by the strong magnetic field to form the filaments. The polarization observations can thus provide a handle on the magnetic field strength of cluster-forming clumps.

Recent polarization observations of cluster-forming clumps show that the global magnetic field lines are more or less spatially well-ordered (e.g., Davis et al. 2000; Houde et al. 2004; Sugitani et al. 2010, 2011). For example, Sugitani et al. (2010) found that the Serpens cloud core is threaded by a hour-glass shaped well-ordered magnetic field and is elongated in the cross-field direction. Sugitani et al. (2011) found that the Serpens South filamentary infrared dark cloud appears to be threaded by more or less straight global magnetic field. The observed spatially-ordered magnetic field structures imply that the magnetic fields in the nearby cluster-forming clumps are likely to be at least

moderately-strong and dynamically important.

4.4. Core Mass Function

In Figs. 15a, 15b, and 15c, we plot the core mass functions (CMFs) for our identified cores for models N1, W1, and S1, respectively. To enlarge the number of sample cores, we added up all the cores identified at the three stages when SFE has reached 0.08, 0.12, and 0.16. In addition, we added up the cores identified from the runs using the different initial turbulent realization for which the different random numbers were used for both the amplitude and phase. The total number of cores so identified is over 500 for each model.

The overall shapes of the CMFs are similar in all three cases, suggesting the shape of the CMF is relatively insensitive to the initial magnetic field strength. This is different from the turbulent fragmentation scenario proposed by Padoan et al. (2001) where a weak magnetic field is required to reproduce the CMF that is similar in shape to the Salpeter IMF (see also Li et al. 2010). In our simulations, a moderately-strong magnetic field can produce a CMF that resembles the Salpeter IMF as well.

We note two interesting features of the computed CMFs. First, there appear to be a lack of massive cores compared to the Salpeter stellar IMF. This is not necessarily a problem, because it is unclear whether the nearby cluster-forming clumps such as ρ Oph and NGC 1333 that we aim to simulate would ever produce massive stars. Alternatively, massive stars can grow from initially less massive cores, fed by global collapsing flows towards the bottom of the clump potential (Smith et al. 2008; Wang et al. 2010). Second, the turnover at the low mass end is less clear in the CMFs than in the Kroupa or Chabrier IMF. This may be because, at the low mass end, most of the cores are gravitationally unbound, and may not form stars. Further studies are required to determine the relation

between the CMF and IMF.

5. Summary

We have performed a set of 3D MHD simulations of cluster formation taking into account the effects of protostellar outflow feedback, and identified dense cores by applying a clumpfind algorithm to the simulated 3D density data cubes. The main results are as follows.

1. Dense cores do not follow Larson’s linewidth-size relation. We find that the velocity dispersions of dense cores show little correlation with core radius, irrespective of the strength of the magnetic field and outflow feedback. In the absence of a magnetic field, the majority of the cores have supersonic velocity dispersions, whereas in the presence of a moderately-strong magnetic field, the cores tend to be subsonic or at most transonic.

2. We find that most of the cores are out of virial equilibrium, with the external pressure due to ambient turbulence dominating the self-gravity. The core formation and evolution is largely controlled by the dynamical compression due to outflow-driven turbulence. Such a situation is contrast to the strongly-magnetized (magnetically subcritical) case, where the self-gravity plays a more important role in the core dynamics, particularly for massive cores.

3. Even an initially-weak magnetic field can retard star formation significantly, because the field is amplified by supersonic turbulence to an equipartition strength. In such an initially weak field, the distorted field component dominates the uniform one. In contrast, for a moderately-strong field, the uniform component remains dominant. Such a difference in the magnetic structure can be observed in simulated polarization maps of dust thermal emission. Recent polarization measurements show that the field lines in nearby cluster-forming clumps are spatially well-ordered, indicative of a moderately-strong,

dynamically-important, field.

This work was supported in part by a Grant-in-Aid for Scientific Research of Japan (20540228 and 22340040) and NASA (NNG06GJ33G and NNX10AH30G). The numerical calculations were carried out mainly on NEC SX9 at the Center for Computational Astrophysics (CfCA) at National Astronomical Observatory of Japan and on NEC SX8 at YITP in Kyoto University.

REFERENCES

- André, P., Belloche, A., Motte, F., & Peretto, N. 2007, *A&A*, 472, 519
- Arce, H. G., Borkin, M. A., Goodman, A. A., Pineda, J. E., & Halle, M. W. 2010, *ApJ*, in press
- Ballesteros-Paredes, J., Gomez, G. C., Pichardo, B., & Vázquez-Semadeni, E. 2009, *MNRAS*, 393, 1563
- Bertoldi, F. & McKee, C. F. 1992, *ApJ*, 395, 140
- Bontemps, S. 2001, *A&A*, 372, 173
- Butler, M. J., & Tan, J. C. 2009, *ApJ*, 696, 484
- Carroll, J. J., Frank, A., Blackman, E. G., Cunningham, A. J., & Quillen, A. C. 2009, *ApJ*, 695, 1376
- Crutcher, R. M., 1999, *ApJ*, 520, 706
- Davis, C. J., Chrysostomou, A., Matthews, H. E., Jenness, T., & Ray, T. P. 2000, *ApJ*, 530, L115
M. 2007, *ApJ*, 61, 262
- Dib, S., Kim, J., Vázquez-Semadeni, E., Burkert, A., & Ahadmehri, M. 2007, *ApJ*, 61, 262
- Di Francesco, J., André, P., & Myers, P. C. 2004, *ApJ*, 617, 425
- Elmegreen, B. G. 2000, *ApJ*, 530, 277
- Federrath, C., Sur, S., Schleicher, D. R. G., Banerjee, R., & Klessen, R. S. 2011, *ApJin* press (axXiv:1102.0266).
- Friesen, R. K., Di Francesco, J., Shimajiri, Y., & Takakuwa, S., 2010, *ApJ*, 708, 1002

- Girart, J. M., Beltrán, M. T., Zhang, Q., Rao, R., & Estalella, R. 2009, *Science*, 324, 1408
- Hartmann, L. W., Ballesteros-Paredes, J., Bergin, E. A. 2001, *ApJ*, 562, 852
- Hennebelle, P., Whitworth, A. P., Gladwin, P. P., & André, P. 2003, *MNRAS*, 340, 870
- Higuchi, A. E., Kurono, Y., Saito, M., & Kawabe, R. 2009, *ApJ*, 705, 468
- Hirota, T. et al. 2008, *PASJ*, 60, 37
- Houde, M. et al. 2004 *ApJ*, 604, 717
- Johnstone, D., Wilson, C. D., Moriarty-Schieven, G., et al. 2000, *ApJ*, 545, 327
- Krumholz, M. R. & McKee, C. F. 2005, *ApJ*, 630, 250
- Klessen, R., Heitsch, F., & Mac Low, M.-M. 2000, *ApJ*, 535, 887
- Krumholz, M. R. & Tan, J. C., 2007, *ApJ*, 656, 959
- Larson, R. B. 1981, *MNRAS*, 194, 809
- Loinard, L., Torres, R. M., Mioduszewski, A. J. & Rodriguez, L. F. 2008, *ApJ*, 675, L29
- Lombardi, M., Lada, C. J. & Alves, J. 2008, *A&A*, 480, 785
- Li, Z.-Y. & Nakamura, F. 2006, *ApJ*, 640, L187
- Li, Z.-Y., Wang, P., Abel, T., & Nakamura, F. 2010, *ApJ*, 720, 26
- Loren, R. T. 1989, *ApJ*, 338, 902
- Mac Low, M.-M., Klessen, R. S., Burkert, A., & Smith, M. D. 1998, *Phys. Rev. Lett.*, 80, 2754
- Mac Low, M.-M. 1999, *ApJ*, 524, 169

- Maruta, H., Nakamura, F., Nishi, R., Ikeda, N., Kitamura, Y. 2010, *ApJ*, 714, 680
- Matsumoto, T., Nakazato, T., & Tomisaka, K. 2006, *ApJ*, 637, L105
- Matthews, B. C., McPhee, C. A., Fissel, L. M., & Curran, R. L. 2009, *ApJS*, 182, 143
- Matzner, C. D., & McKee, C. F. 2000, *ApJ*, 545, 364
- Matzner, C. D. 2007, *ApJ*, 659, 1394
- Maury A., André, P., & Li, Z.-Y. *ApJ*, 2009, 499, 175
- McKee, C. F., & Zweibel, E. G. 1992, *ApJ*, 399, 551
- Motte, F., André, P., & Neri, R. 1998, *A&A*, 336, 150
- Myers, P. C. 2009, *ApJ*, 700, 1609
- Nakamura, F. & Li, Z.-Y. *ApJ*, 2007, 662, 395
- Nakamura, F. & Li, Z.-Y. *ApJ*, 2008, 687, 354
- Nakamura, F. et al. 2011a, *ApJ*, 726, 46
- Nakamura, F. et al. 2011b, *ApJ*, in press (arXiv:1105.4481)
- Nakano, T., & Nakamura, T. 1978, *PASJ*, 30, 681
- Ostriker, E. C., Stone, J. M., & Gammie, C. F., 2001, *ApJ*, 546, 980
- Padoan, P., Goodman, A., Draine, B. T., Juvela, M., Nordlund, A., & Rognvaldsson, O. E.
2001, *ApJ*, 559, 1005
- Padoan, P. & Nordlund, A. 2002, *ApJ*, 576, 870
- Pelkonen, V.-M., Juvela, M., & Padoan, P. 2007, *A&A*, 461, 551

- Price, D. J., & Bate, M. R. 2008, MNRAS, 385, 1820
- Price, D. J., & Bate, M. R. 2009, MNRAS, 398, 33
- Rathborne, J. M., Jackson, J. M., & Simon, R. 2006, ApJ, 641, 389
- Ridge, N. A., Wilson, T. L., Megeath, S. T., Allen, L. E., & Myers, P. C. 2003, AJ, 126, 286
- Smith, R. J., Clark, P. C., & Bonnell, I. A. 2008, MNRAS, 391, 1091
- Stanke, T., Smith, M. D., Gredel, R., & Khanzadyan, T. 2006, A&A, 447, 609
- Sugitani, K., Nakamura, F., Tamura, M., Watanabe, M., Kandori, R., Nishiyama, S.,
Kusakabe, N., Hashimoto, J., Nagata, T., & Sato, S. 2010, ApJ, 716, 299
- Sugitani, K. et al. 2011, ApJ, 734, 63
- Testi, L. & Sergent, A. 1998, ApJ, 508, L91
- Tilley, D., & Pudritz, R. 2007, MNRAS, 382, 73
- Walsh, A. J., Myers, P. C., Di Francesco, J., Mohanty, S., Bourke, T. L., Gutermuth, R. &
Wilner, D. 2007, ApJ, 655, 958
- Wang, P., Li, Z.-Y., Abel, T., & Nakamura, F. 2010, ApJ, 709, 27
- Williams, J. P., de Geus, E. J., & Blitz, L. 1994, ApJ, 428, 693

A. Star Formation Rate in A Cluster Forming Clump

Using 3D MHD numerical simulations of cluster formation, Li & Nakamura (2006) and Nakamura & Li (2007) demonstrated that the protostellar outflow-driven turbulence can keep a pc-scale, cluster-forming clump close to a virial equilibrium long after the initial turbulence has decayed away. Here, we derive an analytic formula of star formation rate in a cluster-forming clump that keeps its virial equilibrium by the protostellar outflow feedback.

Numerical simulations of protostellar turbulence indicate that the dissipation rate of the turbulence momentum, dP_{turb}/dt , balances the momentum injection rate by the protostellar outflow feedback, dP_{out}/dt , so that the clump can be kept close to a virial equilibrium,

$$\frac{dP_{\text{turb}}}{dt} = \frac{dP_{\text{out}}}{dt} . \quad (\text{A1})$$

The dissipation rate of the turbulence momentum, dP_{turb}/dt , can be written as

$$\frac{dP_{\text{turb}}}{dt} = \alpha \frac{M_{\text{cl}} V_{\text{vir}}}{t_{\text{diss}}} , \quad (\text{A2})$$

where $\alpha \sim 0.5$ (Mac Low 1999). The virial velocity, V_{vir} , is given by

$$V_{\text{vir}} = \sqrt{\frac{3}{5} a f_{\text{B}} \frac{GM_{\text{cl}}}{R_{\text{cl}}}} . \quad (\text{A3})$$

The momentum dissipation time is $t_{\text{diss}} = R_{\text{cl}}/V_{\text{vir}}$. The dimensionless parameter of order unity, a , measures the effects of a nonuniform or nonspherical mass distribution. For a uniform sphere and a centrally-condense sphere with $\rho \propto r^{-2}$, $a = 1$ and $5/3$, respectively. In the following analysis, we adopt $a = 5/3$ because the cluster-forming clumps tend to be centrally-condensed. We take into account the magnetic support by multiplying the virial velocity by a factor f_{B} , where $0 \lesssim f_{\text{B}} \lesssim 1$.

The momentum injection rate by the protostellar outflows is given by

$$\frac{dP_{\text{out}}}{dt} = \epsilon_{\text{SFR}} \times f_{\text{w}} V_{\text{w}} , \quad (\text{A4})$$

where V_w is the flow speed and ϵ_{SFR} is the star formation rate. Using equations (A1) and (A4), the star formation rate is rewritten as

$$\epsilon_{\text{SFR}} = \frac{3}{5} a \alpha f_B f_w^{-1} V_w^{-1} \frac{GM_{\text{cl}}^2}{R_{\text{cl}}^2}. \quad (\text{A5})$$

If we normalize ϵ_{SFR} to $M_{\text{cl}}/t_{\text{ff}}$, then the star formation efficiency per free-fall time is given by

$$\text{SFR}_{\text{ff}} = \epsilon_{\text{SFR}} \frac{t_{\text{ff}}}{M_{\text{cl}}} \simeq 0.0125 \alpha \left(\frac{f_B}{0.5} \right) \left(\frac{f_w}{0.5} \right)^{-1} \left(\frac{V_w}{10^2 \text{ km s}^{-1}} \right)^{-1} \left(\frac{R_{\text{cl}}}{1 \text{ pc}} \right)^{1/2} \left(\frac{\Sigma_{\text{cl}}}{5 \times 10^{21} \text{ cm}^{-2}} \right)^{1/2}, \quad (\text{A6})$$

where the surface density is $\Sigma = M_{\text{cl}}/\pi R_{\text{cl}}^2$ and the free-fall time is $t_{\text{ff}} = \sqrt{3\pi/32G\rho}$.

Figure 16 shows the dependence of SFR_{ff} on the mass and radius, obtained from the above equation. The crosses and diamonds indicate the cluster-forming clumps observed in the C^{18}O ($J = 1 - 0$) line by Ridge et al. (2003) and Higuchi et al. (2009), respectively. Our model suggests that the star formation rate per free-fall time ranges from 1 % to 5 % for the observed cluster-forming clumps in the solar neighborhood when the protostellar outflow feedback maintains the supersonic turbulence in the clumps, indicating that it takes about $(2 - 10) t_{\text{ff}}$ for the star formation efficiency to reach about $(10 - 20)$ %.

Table 1. Model Characteristics

Model	β	f^a	Remark
N1	∞	0.4	no B field
N2	∞	0.0	no B field, no feedback
W1	2	0.4	weak B field
W2	2	0.0	weak B field, no feedback
S1	0.2	0.4	moderately-strong B field
S2	0.2	0.0	moderately-strong B field, no feedback
S3	0.2	0.1	moderately-strong B field, weak feedback

^aoutflow strength

Table 2. Summary of the Physical Properties of the identified cores

Property	Minimum	Maximum	Mean ^a	Median
model N1				
R_c (pc)	0.013	0.041	0.020 ± 0.005	0.020
M_c (M_\odot)	0.075	3.51	0.67 ± 0.67	0.40
ΔV_{NT} (km s^{-1})	0.13	4.53	1.06 ± 0.77	0.86
model W1				
R_c (pc)	0.013	0.034	0.020 ± 0.006	0.019
M_c (M_\odot)	0.076	3.90	0.62 ± 0.77	0.31
ΔV_{NT} (km s^{-1})	0.13	14.4	0.99 ± 1.66	0.47
model S1				
R_c (pc)	0.013	0.048	0.024 ± 0.008	0.023
M_c (M_\odot)	0.073	4.39	0.86 ± 1.03	0.47
ΔV_{NT} (km s^{-1})	0.086	2.64	0.46 ± 0.52	0.31

^aWith standard deviation

Note. — The gas temperature is assumed to be $T = 20$ K, corresponding to the sound speed of 0.266 km s^{-1} .

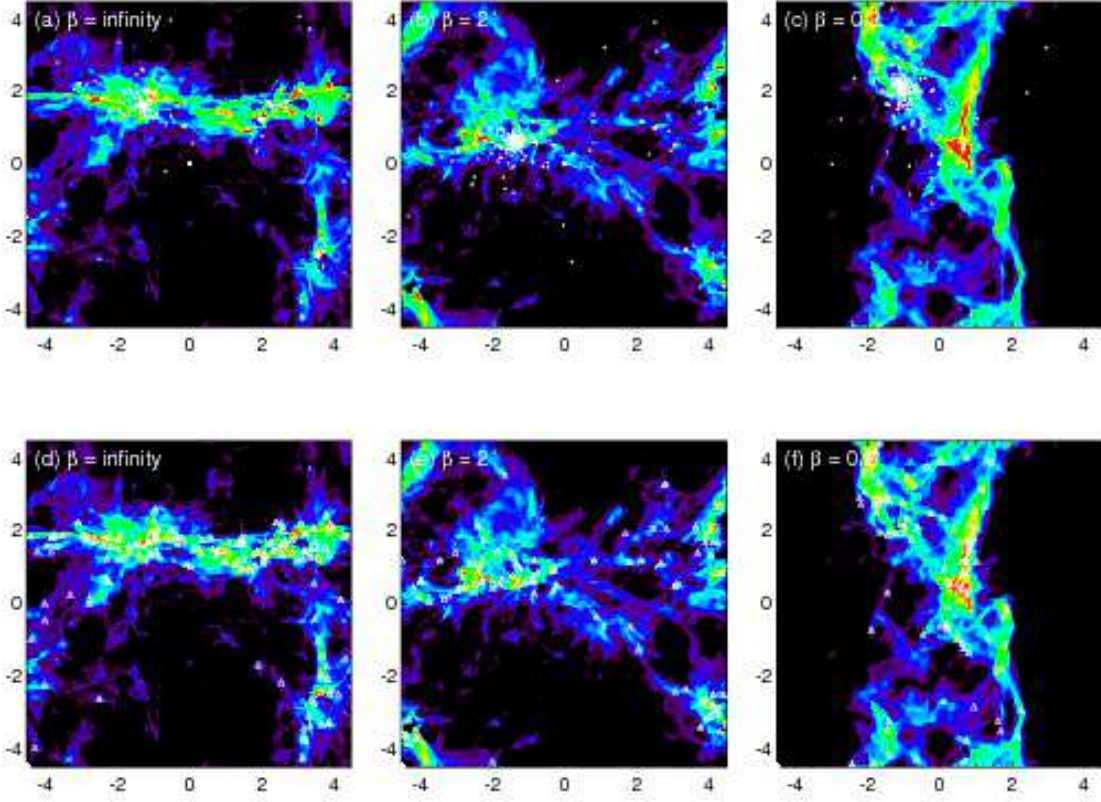


Fig. 1.— Column density snapshots on the x - z plane for (a) model N1 ($t = 4.6t_{\text{ff},c} \sim 0.9$ Myr), (b) W1 ($t = 6.5t_{\text{ff},c} \sim 1.2$ Myr), and (c) S1 ($t = 7.4t_{\text{ff},c} \sim 1.4$ Myr) at the stage when 16 % of the total mass has been converted into stars. The positions of the formed stars are overlaid with the dots. The units of length are the central Jeans length $L_J = (\pi c_s^2 / G \rho_0)^{1/2} \simeq 0.17(T/20\text{K})^{1/2}(n_{\text{H}_2,0}/2.69 \times 10^4 \text{cm}^{-3})^{-1/2}$ pc. The initial magnetic field direction is parallel to the x -axis. In panels (d) through (f), the positions of the identified cores are overlaid with the triangles on the same column density images as those shown in panels (a) through (c).

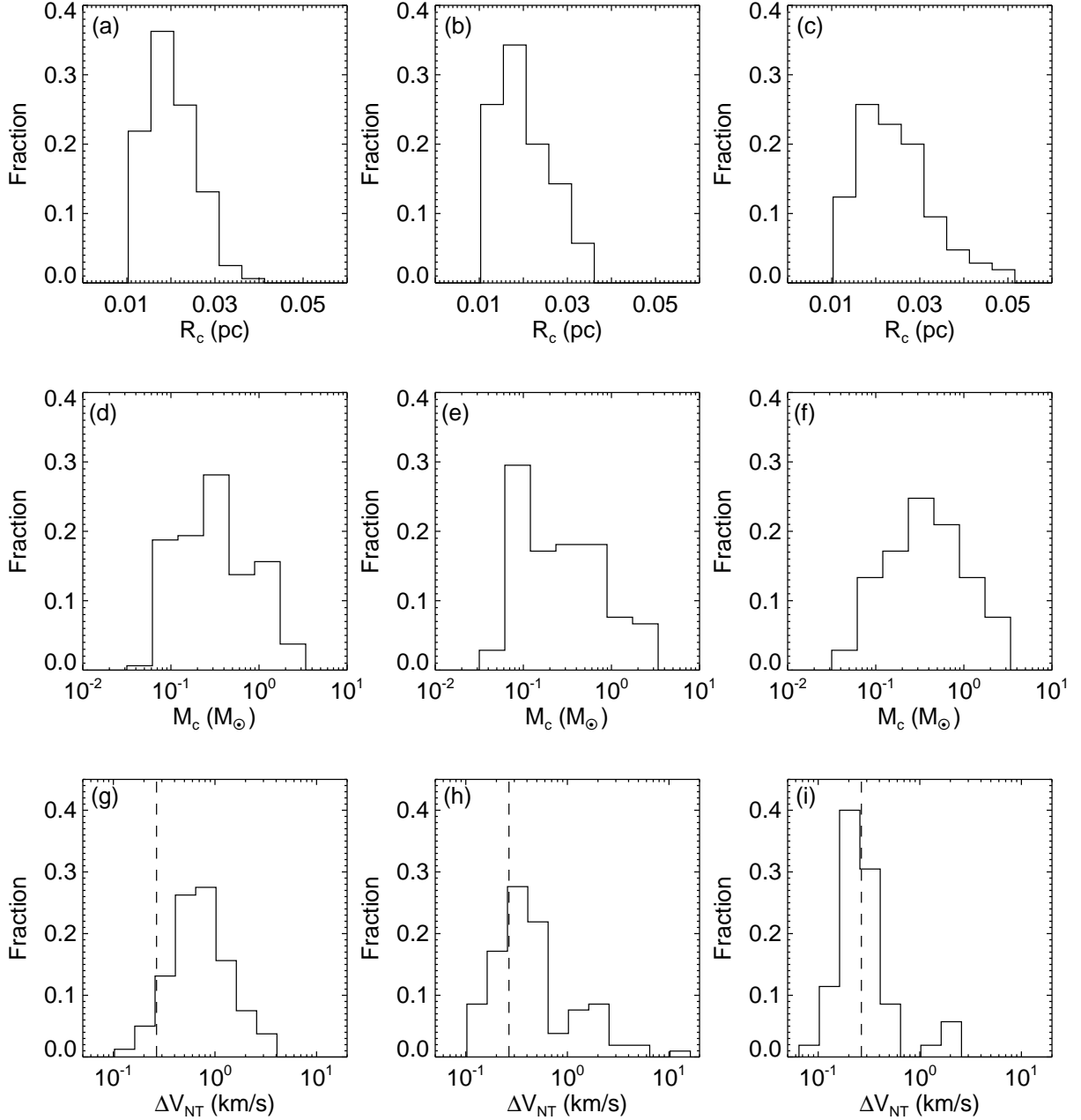


Fig. 2.— Histograms of some physical quantities of the identified cores. They are plotted at the same stages as those of Fig. 1. Panels (a), (b), and (c) are the histograms of the core radius for models N1, W1, and S1, respectively. Panels (d), (e), and (f) are the histograms of the core mass for models N1, W1, and S1, respectively. Panels (g), (h), and (i) are the histograms of the 3D velocity dispersion of the nonthermal component for models N1, W1, and S1, respectively. The vertical dashed lines indicate the sound speed with gas temperature of 20 K.

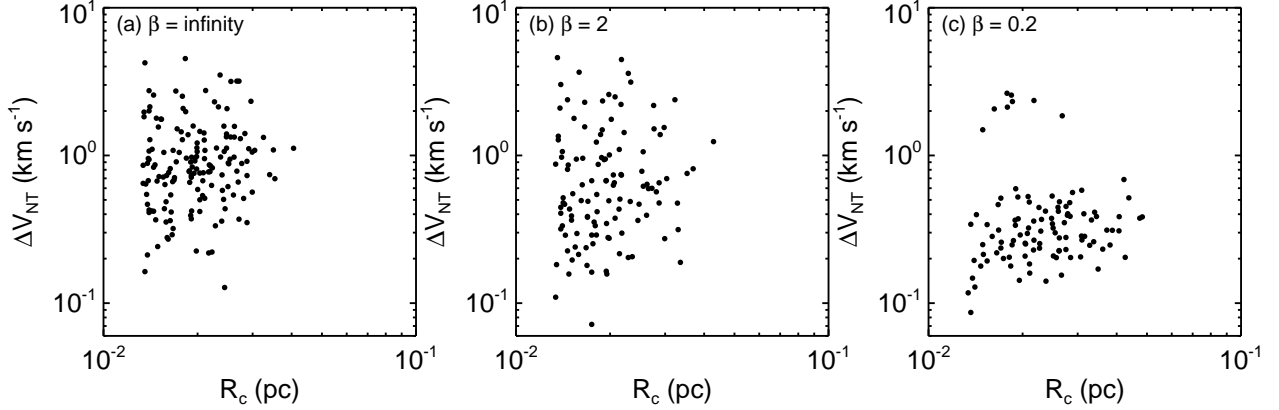


Fig. 3.— Nonthermal 3D velocity dispersions as a function of core radii for three models with different magnetic field strengths: (a) model N1, (b) model W1, and (c) model S1. They are plotted at the same stages as those of Fig. 1. The sound speed is $c_s = 0.266 \text{ km s}^{-1}$, corresponding to $T = 20 \text{ K}$.

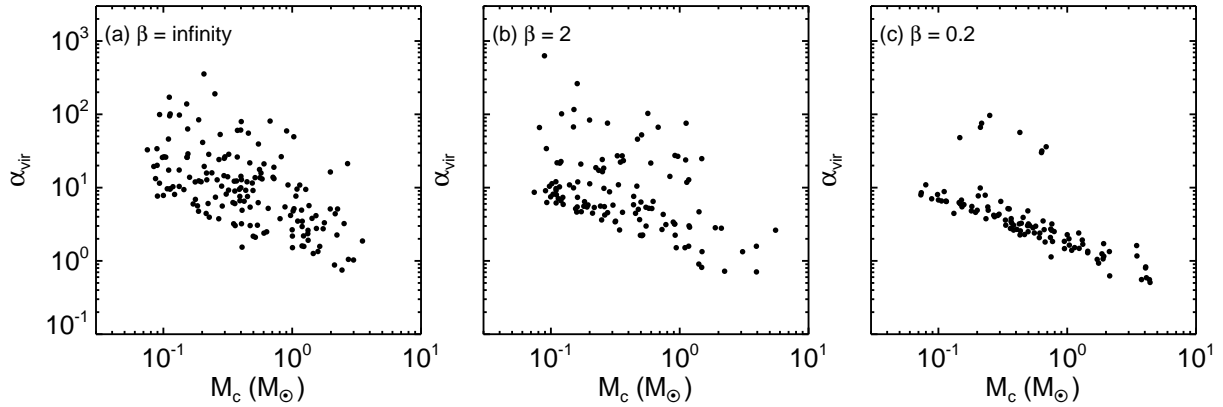


Fig. 4.— Virial parameters as a function of core masses for three models with different magnetic field strengths: (a) model N1, (b) model W1, and (c) model S1. They are plotted at the same stages as those of Fig. 3.

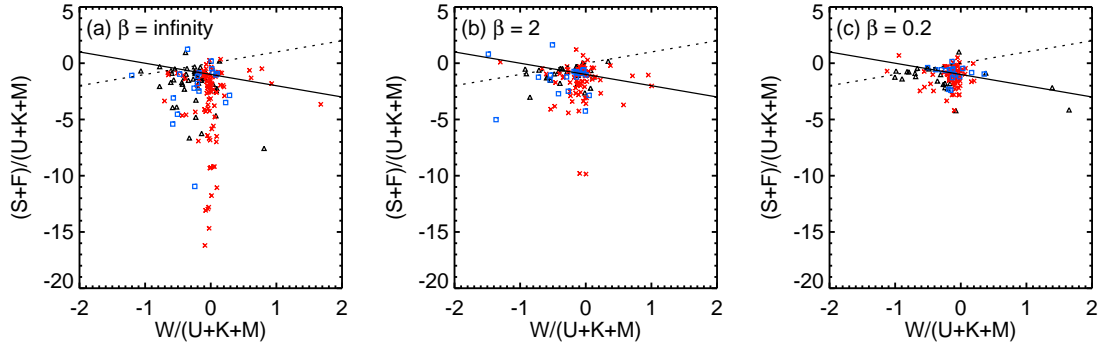


Fig. 5.— Relationship between the sum of the two surface terms, $S+F$, and the gravitational term, W , in the virial equation. They are normalized to the sum of the internal terms, $U + K + M$. The solid line indicates the virial equilibrium, $U + K + W + S + M + F = 0$. They are plotted at the same stages as those of Fig. 3. The dashed line indicates the line below which the surface term is larger than the gravitational term. For the cores that lie below the solid line, the left-hand side of the virial eq. 2 is negative and thus expected to be bound. All others that lie above the solid line are unbound and expected to disperse away, if they do not gain more mass through accretion and/or merging with other cores, or reduce internal support through turbulence dissipation. A red cross, black triangle, and blue square indicates a core with mass of $M_c \leq 0.75 \langle M_c \rangle$, $0.75 \langle M_c \rangle \leq M_c \leq 1.25 \langle M_c \rangle$, and $M_c \geq 1.25 \langle M_c \rangle$, respectively. The close-up of Fig. 5c is presented in Fig. 7c.

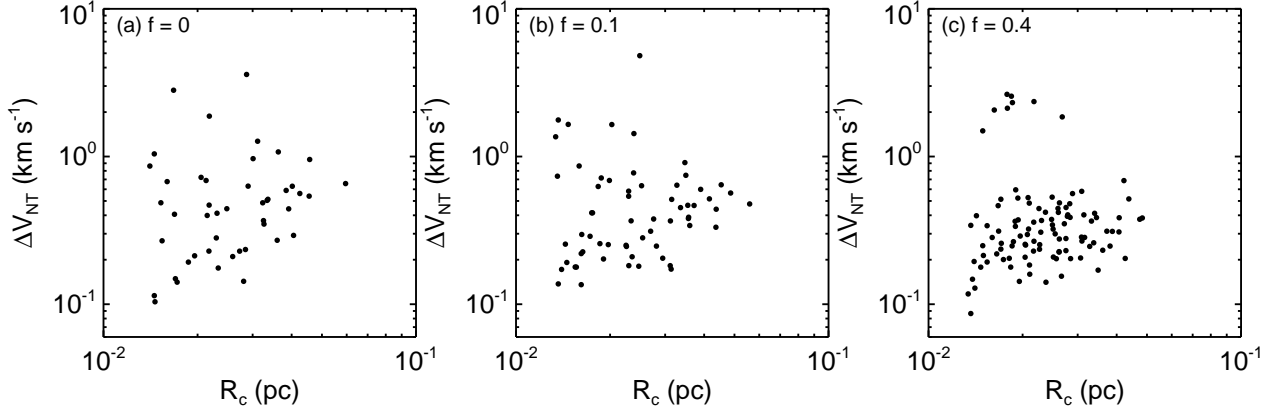


Fig. 6.— Same as Fig. 3 but for models (a) S3, (b) S2, and (c) S1.

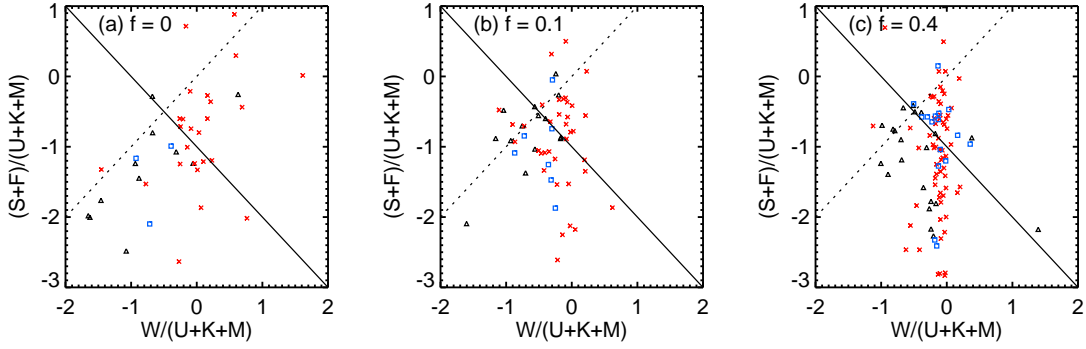


Fig. 7.— Same as Fig. 5 but for models (a) S3, (b) S2, and (c) S1.

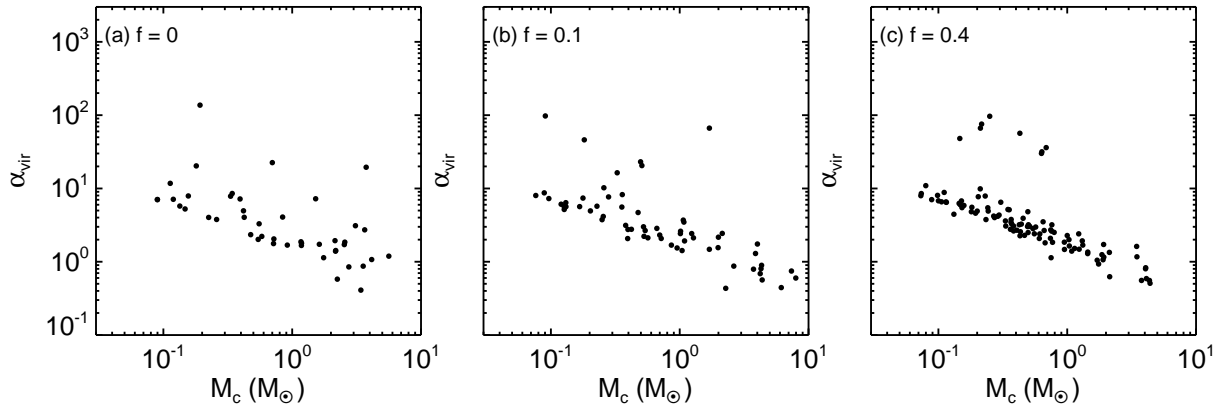


Fig. 8.— Same as Fig. 4 but for models (a) S3, (b) S2, and (c) S1.

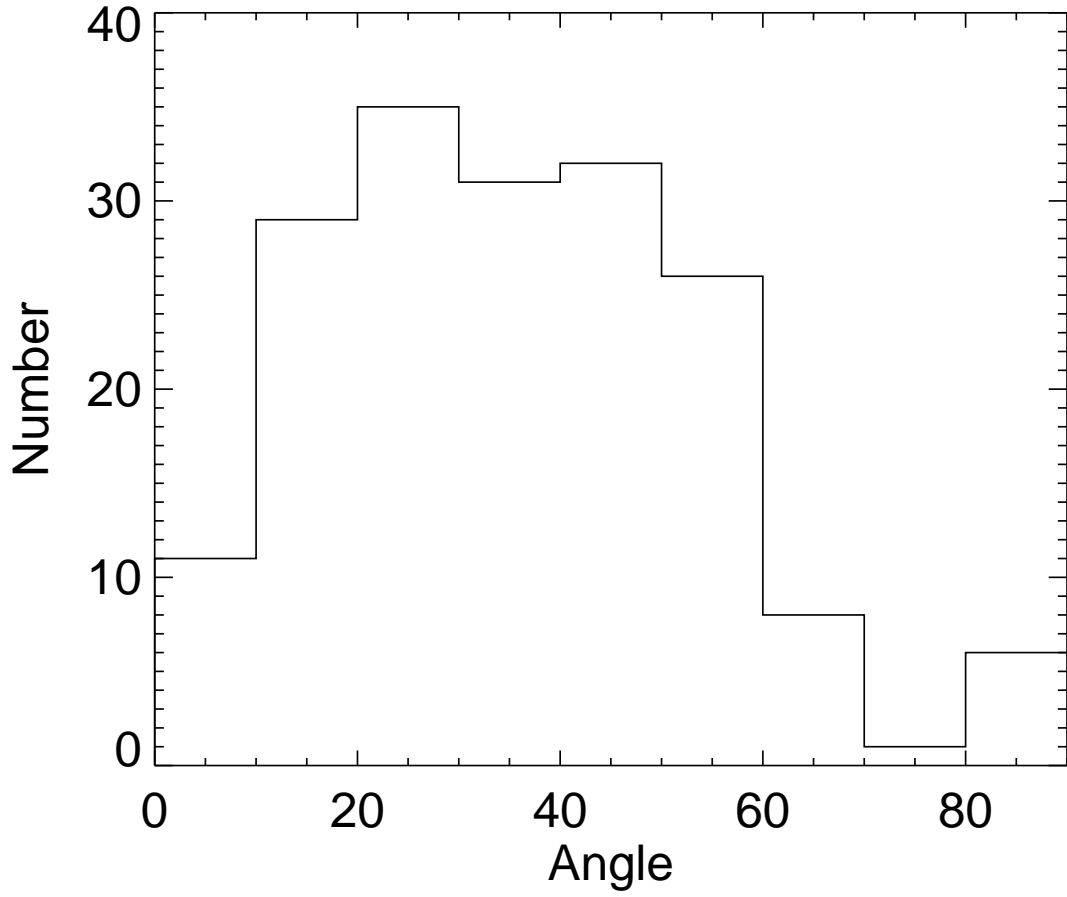


Fig. 9.— Histogram of the outflow direction relative to the initial magnetic field direction for the model with a moderately-strong magnetic field (model S1).

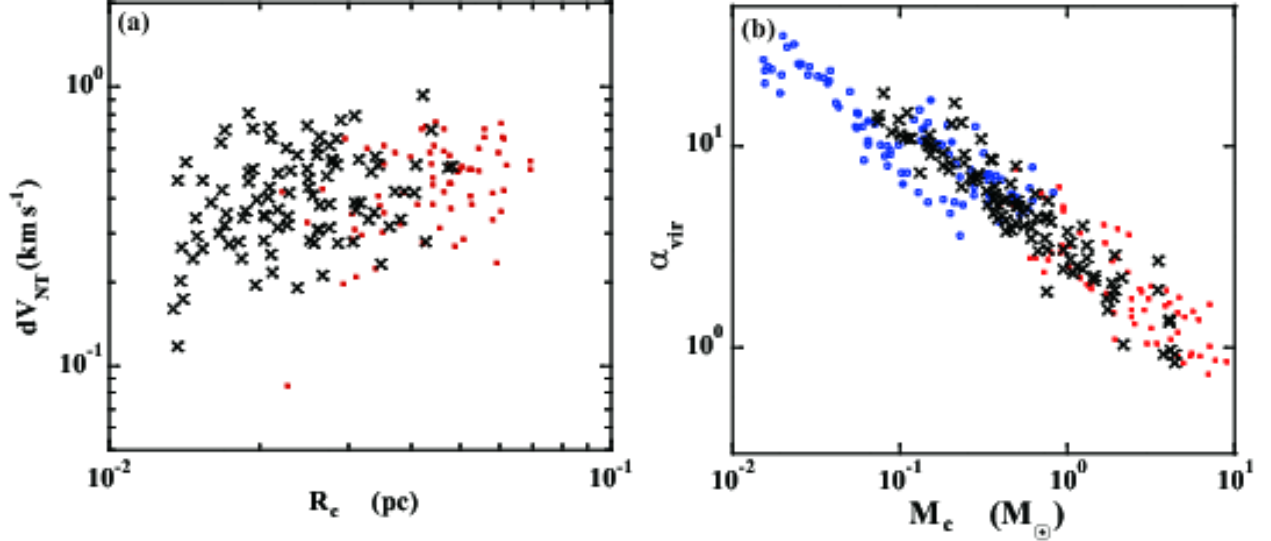


Fig. 10.— (a) the relationship between the 1D FWHM nonthermal velocity width and core radius for the dense cores in the ρ Ophiuchi Main Cloud and our cores identified from the moderately-strong magnetic field model (model S1). The red dots and black crosses denote the ρ Oph cores and our cores of model S1, respectively. For the ρ Oph cores, we used the results of Maruta et al. (2010) who identified the cores using H^{13}CO^+ ($J = 1 - 0$) data. For our cores of model S1, we recalculated the 1D FWHM velocity widths from the 3D core velocity dispersions derived in Section 3. (b) The virial parameter-core mass relation. The red dots and black crosses are the same as those of panel (a). The blue open circles denote the cores of NGC 1333 identified using N_2H^+ ($J = 1 - 0$) emission (Walsh et al. 2007). For ρ Oph cores and NGC 1333 cores, the LTE masses are adopted as the core masses. For the NGC 1333 cores, we recalculated the LTE masses derived by (Walsh et al. 2007) by assuming the average N_2H^+ fractional abundance relative to H_2 obtained toward ρ Oph of $X_{\text{N}_2\text{H}^+} \sim 3 \times 10^{-10}$ and distance of 250 pc. See the text for detail.

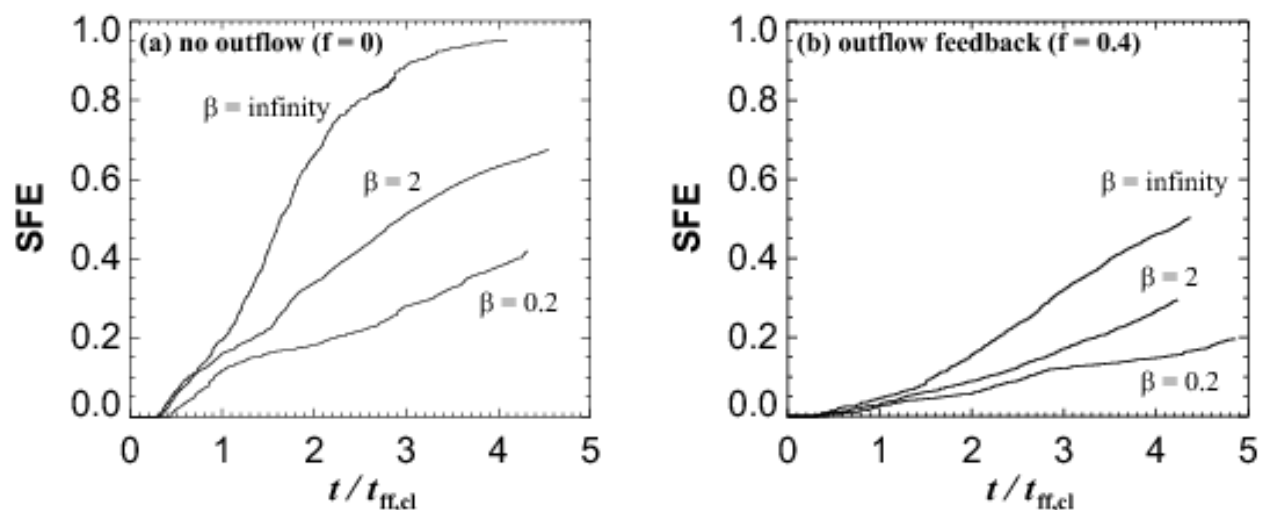


Fig. 11.— (a) Time evolution of star formation efficiencies for three models with no outflow feedback. The three models have different initial magnetic field strengths: models N2 ($\beta = \infty$), W2 ($\beta = 2$), and S2 ($\beta = 0.2$). The evolution time is normalized to the global clump free-fall time, $t_{\text{ff,cl}} = 0.49(L/1.5\text{pc})(20\text{K}/T)^{1/2}$ Myr. (b) Same as panel (a) but for models with outflow feedback (models N1, W1, and S1).

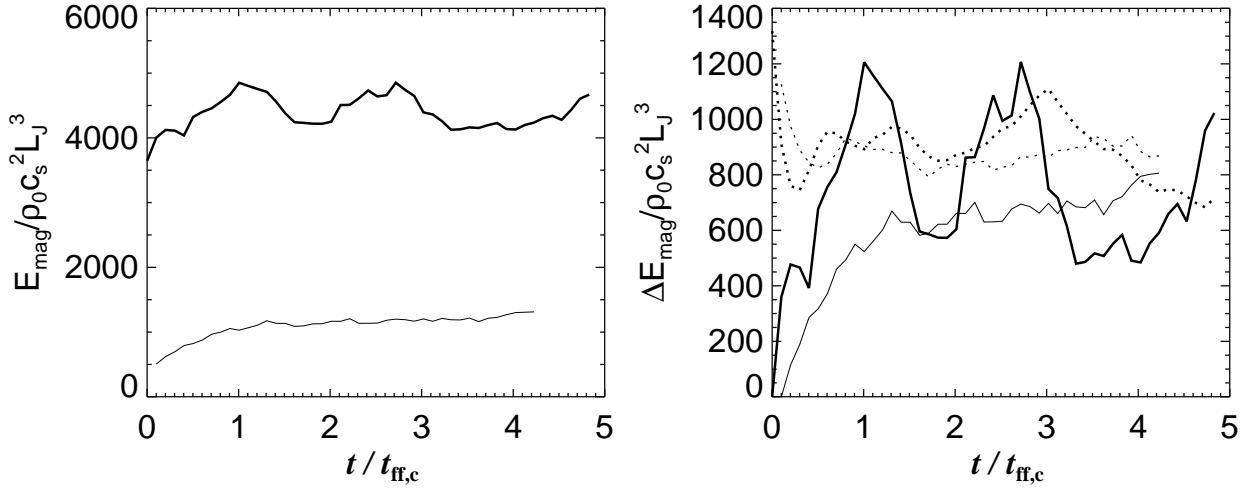


Fig. 12.— (a) Time evolution of total magnetic energy for two models with different initial magnetic field strengths. Thick and thin lines are for the models with moderately-strong (model S1) and weak magnetic field (model W1), respectively. The evolution time is normalized to the global clump free-fall time, $t_{\text{ff,cl}} = 0.49(L/1.5\text{pc})(20\text{K}/T)^{1/2}$ Myr. (b) Time evolution of magnetic energy of amplified component (solid lines) and kinetic energy of turbulence (dotted lines). The magnetic energy of the amplified component tends to approach the kinetic energy for each model.

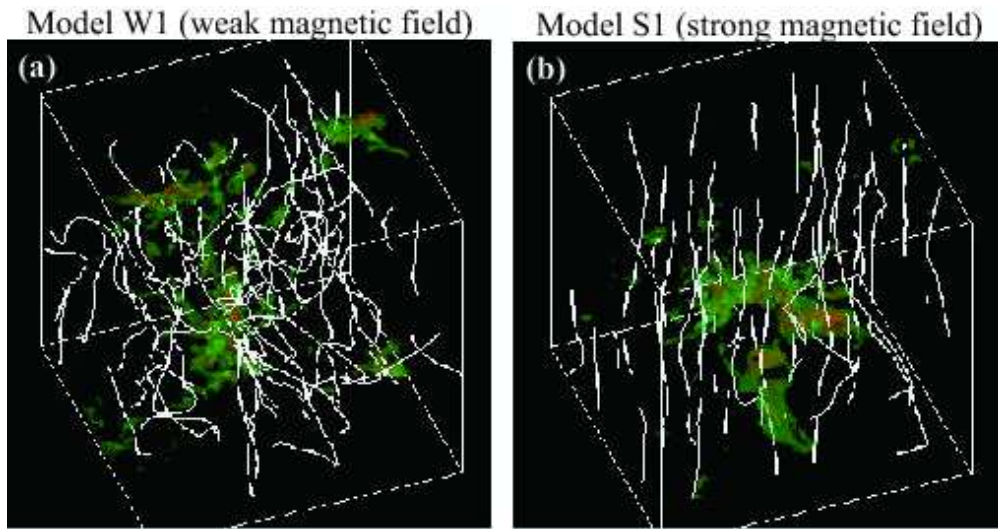


Fig. 13.— 3D view of the density and magnetic field distributions for (a) the weakly-magnetized model (model W1) and (b) the strongly-magnetized model (model S1) at the stage where the star formation efficiency has reached 0.16. The color images indicate the isodensity surfaces. The white curves are the magnetic field lines. For both the panels, only the central $L/2 \times L/2 \times L/2$ region is shown.

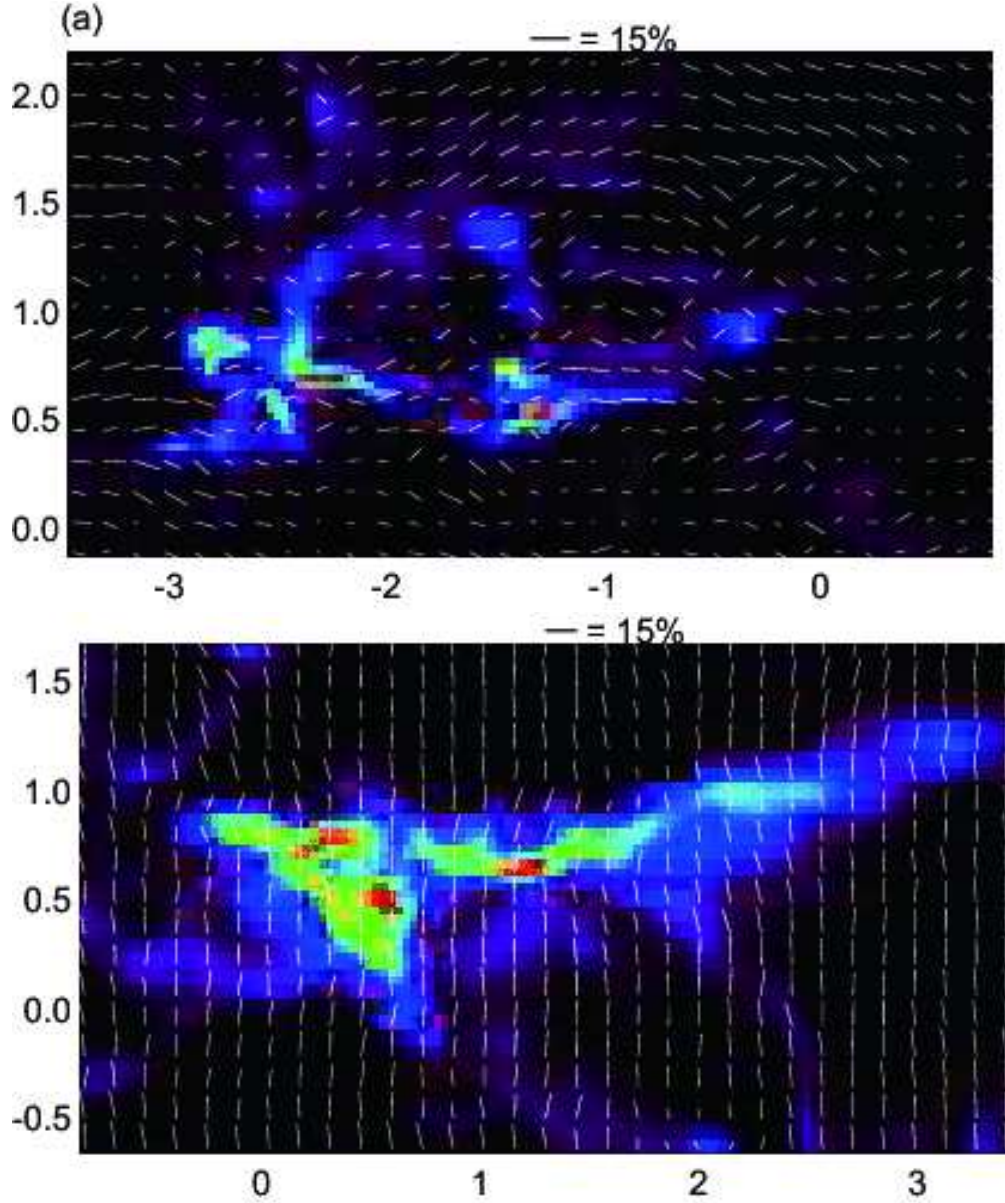


Fig. 14.— (a) Polarization maps of (a) model W1 (weak magnetic field) and (b) model S1 (moderately-strong magnetic field). The length of a polarization vector is proportional to the degree of polarization, with the longest vector corresponding to $P = 15\%$. Only one polarization vector is plotted for every four computational cells. The color contour shows the column density distribution. The initial magnetic field lines are parallel and perpendicular to the horizontal line for panels (a) and (b), respectively. The units of length are the central Jeans length $L_J = (\pi c_s^2 / G \rho_0)^{1/2} \simeq 0.17 (T / 20 \text{K})^{1/2} (n_{\text{H}_2,0} / 2.69 \times 10^4 \text{cm}^{-3})^{-1/2}$ pc.

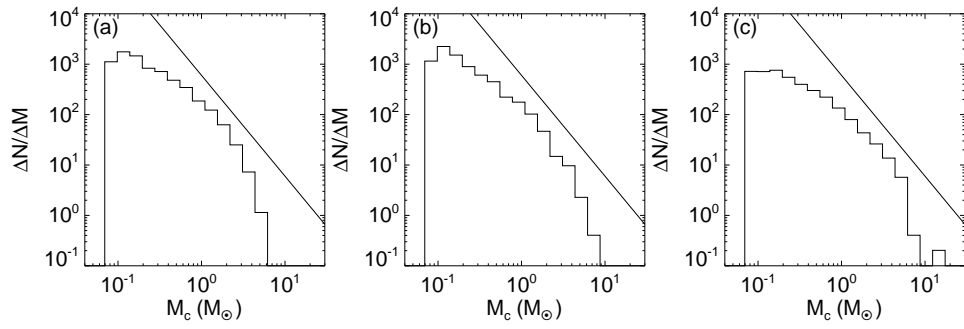


Fig. 15.— Core mass functions for (a) model N1, (b) model W1 and (c) model S1. A power-law of $\Delta N/\Delta M \propto M^{-2}$ is plotted for comparison.

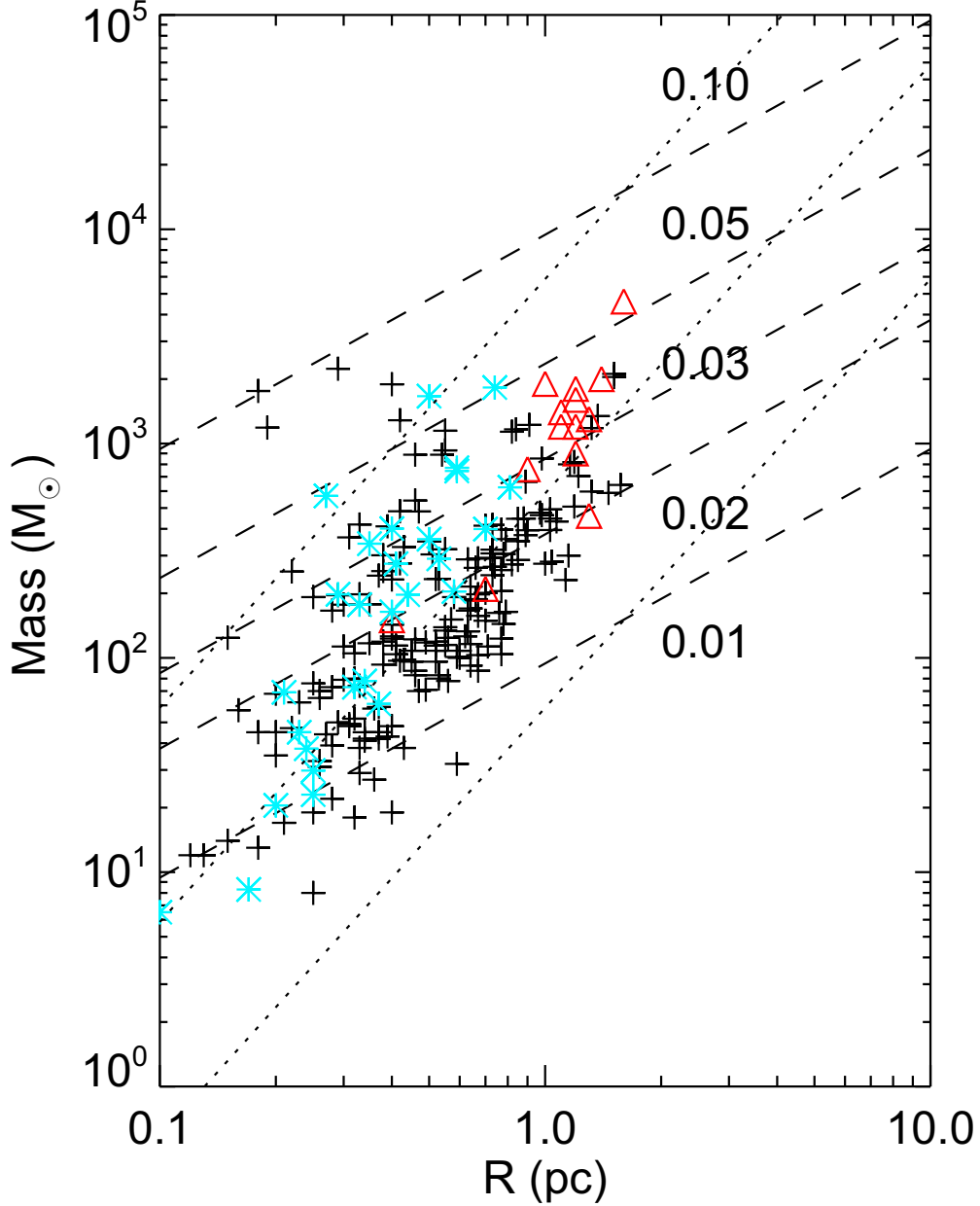


Fig. 16.— Contours of star formation rate per free-fall time predicted by the outflow-regulated cluster formation model on the mass-radius diagram. The dashed contours are labeled by values of SFR_{ff} . The dotted contours indicate the constant column density at 10^{21} cm^{-2} (*bottom line*), 10^{22} (*intermediate line*), and 10^{23} cm^{-2} (*upper line*). The crosses and triangles indicate the cluster-forming dense clumps identified by Ridge et al. (2003) and Higuchi et al. (2009) in C^{18}O ($J = 1 - 0$), respectively. The asterisks indicate the dense clumps in the infrared dark clouds identified by Rathborne et al. (2003). For most of the dense clumps, the predicted SFR_{ff} ranges from 1 % to 5 %, indicative of slow star formation.